



Full length article

A moiré theory for probing grain boundary structure in graphene

Emil Annevelink^a, Zhu-Jun Wang^{b,c,*}, Guocai Dong^{d,e}, Harley T. Johnson^{a,f}, Pascal Pochet^{g,*}^a Department of Mechanical Science and Engineering, University of Illinois at Urbana-Champaign, Urbana IL 61801 USA^b Scientific Center for Optical and Electron Microscopy, ETH Zurich, Otto-Stern-Weg 3, 8093 Zurich, Switzerland^c School of Physical Science and Technology, Shanghai Tech University, Shanghai 201210, P.R. China^d Kamerlingh Onnes Laboratory, Leiden University, P.O. Box 9504, 2300 RA Leiden, The Netherlands^e GC Innovation Co., Ltd. No.8 Lanxiang Road, Changzhou, Jiangsu, P.R. China^f Department of Materials Science and Engineering, University of Illinois at Urbana-Champaign, Urbana IL 61801 USA^g Department of Physics, IRIG, Univ. Grenoble Alpes and CEA, F-38000 Grenoble, France

ARTICLE INFO

Article history:

Received 17 March 2021

Revised 25 June 2021

Accepted 4 July 2021

Available online 21 July 2021

Keywords:

Graphene growth

Grain boundary

Coalescence

Moiré metrology

In-operando STM

ABSTRACT

Multiscale microscopy spanning the atomistic, moiré, and meso scales has enabled engineering the equilibrium structure of graphene. However, temporal restrictions on in-operando imaging techniques make the moiré scale the finest accessible spatial resolution, thereby limiting our understanding of atomistic mechanisms of non-equilibrium processes in graphene. In order to include atomic scale features with in-operando microscopy, we develop a moiré metrology theory that infers the atomic scale structure from the moiré scale, creating a bridge to in-operando microscopy. The theory is based on atomic scale models that govern the atomistic structure and are promoted to the moiré scale by simulation. We introduce this through a relevant application: nuclei coalescence of graphene during chemical vapor deposition. We develop two mechanistic atomic scale models that govern the propagation and structure of grain boundaries, illuminating how edge dislocations, disconnections, and grain boundaries form from the attachment of individual dimers. The atomistic models are brought to the moiré scale through bond convolution simulations and the resultant moiré metrology theory is tested on results from in-operando scanning tunneling microscopy. By showing that we can identify atomic scale defects from moiré patterns, we highlight how moiré metrology can enable decision making during growth from in-operando observation of graphene structure, paving the way for the design of graphene atomistic structure under scalable synthesis conditions.

© 2021 Acta Materialia Inc. Published by Elsevier Ltd. All rights reserved.

1. Introduction

Designing the atomistic structure of graphene is critical to manufacturing devices with desired mechanical [1–3], thermal [4], and electrical properties [5,6]. One reason engineering the atomic structure has been elusive is a lack of in-operando imaging techniques that reveal atomic scale details under working conditions. For instance, in-operando atomic scale microscopy of the formation of graphene grain boundaries, which contain the bulk of topological defects in graphene, is not possible with current technologies due to incompatibilities in spatial and temporal acquisition rates. Therefore, the mechanisms underlying dramatic changes in graphene grain boundary structure due to small variations [7–10] in

the synthesis procedure during the primary manufacturing method for large-area graphene chemical vapor deposition (CVD) remain largely unknown [11]. We aim to address this limitation by introducing a moiré theory that uses the moiré patterns visible in experiments and simulations to bridge the atomic and nano scales.

Moiré patterns arise due to lattice mismatch in periodic systems and can be formed by stretching or twisting one lattice relative to another [12]. The relative mismatch between two lattices are networks of topological defects [13] and have been observed for decades in thin-film growth [14,15] and more recently in systems containing two-dimensional materials [16]. The relative mismatch can be expressed mathematically to find a given moiré pattern between two arbitrary lattices [17]. For graphene-metal systems, where the lattice mismatch is between five and ten percent, the moiré pattern is roughly five nanometers and has been confirmed experimentally [18,19].

* Corresponding author.

E-mail addresses: wangzhj3@shanghaitech.edu.cn (Z.-J. Wang), pascal.pochet@cea.fr (P. Pochet).

Since the moiré pattern is a topological property of the lattices, it is sensitive to changes in the topology of either lattice. This means that topological defects like dislocations or grain boundaries in either lattice appear in the moiré pattern [20]. We believe that changes to the moiré structure can be used for metrology to promote atomic scale insights to nanoscale. Here we develop a moiré theory that can be utilized in conjunction with moiré sensitive microscopy to extend standard microscopy techniques to enable in-operando metrology of the evolving grain boundary structure during graphene growth.

The standard approach for studying graphene atomic structure uses sequential imaging of the equilibrium structure via complementary microscopy techniques that span multiple scales. For example, scanning electron microscopy (SEM) reveals mesoscale details of graphene nucleation density and grain size to show the influence of CVD growth conditions on various substrates [21]. Scanning transmission electron microscopy (STEM) and dark-field transmission electron microscopy (dfTEM) show angstrom-to-micron details of the grain boundary structure and patchwork of grains to control the defect density in graphene [16,22,23]. Scanning tunneling microscopy (STM), meanwhile, shows angstrom-to-nanoscale details of the structure and electronic properties [24]. These microscopy techniques, when stitched together, create a multiscale understanding of graphene growth that has dramatically improved the quality of graphene [25]. However, equilibrium microscopy only characterizes the microstructure after growth, which inherently limits control and design of the atomic structure because there is no understanding or observation of the dynamic growth process or the mechanisms involved.

In-operando microscopy techniques enable observation of non-equilibrium CVD growth mechanisms, paving the way for dynamic control. Recently, a number of such microscopy techniques have been used to reveal details of graphene synthesis [26–28]. We focus on in-operando STM since we are interested in the role of moiré patterns (see Supplementary Video 1). In-operando STM has revealed moiré-unit growth of graphene, whereby graphene clusters are grown 144 carbon atoms at a time[29]. In addition, in-operando STM has shown that carbon predominantly attaches to concave corners during coalescence[30]. To study growth, microscopy techniques need to be fast enough, and over sufficiently large areas. Unfortunately, this renders in-operando atomic resolution microscopy impossible, making the nanometer scale of the moiré pattern the highest possible resolution with current technology. In order to reveal the atomic scale, a technique is needed that can reveal atomic scale features from a larger scale through a “top-bottom” scale-bridging analysis.

We address this limitation by developing a moiré theory that bridges experiment and simulation to reveal atomistic features from moiré scale microscopy, which we introduce by applying it to the formation of grain boundaries during CVD synthesis.

In this work, we model and image graphene grown on rhodium to benefit from the strong coupling that amplifies the moiré signal. Besides the strong coupling, nothing in the modeling is limited by choosing rhodium as a substrate since only the growth surface lattice (triangular) and the lattice constant are taken into account. Rhodium is also a model system for strongly interacting substrates like the new Cu-Ni alloys which show greater control of graphene growth [31], but recent examples of aligned graphene growth on copper allude to the expansion of this approach to weakly interacting substrates [32]. The moiré theory uses atomic scale simulations to determine grain boundary formation mechanisms, which are brought to the moiré scale through bond-convolution simulations. It maintains a wide field of view and addresses the current incompatibility between temporal and spatial acquisition rates as well as establishes the next frontier of graphene growth analysis

by removing the uncertainty surrounding defects that occur during growth.

2. Methods

2.1. Monte carlo simulations

The moiré theory contains atomic scale mechanistic models which are developed through a Monte Carlo framework implemented in python to grow grain boundaries. The Monte Carlo algorithm finds all the carbon atoms that do not have three nearest neighbors according to a bond-length cutoff. The under-coordinated carbon atoms within three bond lengths are paired and carbon dimers are added to propose growth steps. The proposed topologies are checked to ensure the added dimer forms a five, six, seven, or eight atom carbon ring to limit energy evaluations.

The energy of each proposed topology is calculated with classical force fields in the LAMMPS package[33]. The energy of the carbon atoms are found using a reactive potential that was parameterized for graphitic structures[34]. Hydrogen atoms are used to terminate carbon atom at the edge of graphene flakes to ensure all carbon atoms have the same bonding type. A substrate interaction is included through a model Lennard-Jones force field, where edge atoms and bulk atoms are treated differently to mirror the covalent bonding at the edge. Bulk LJ parameters are ϵ_b : 0.01eV and σ_b : 2.6Å and edge parameters are ϵ_e : 1eV and σ_e : 2.6Å, which are found according to the procedure in [Appendix A](#).

2.2. In-situ scanning tunneling microscopy

The moiré theory is compared to in situ STM observations performed on Rh(111) under low-vacuum conditions within an STM that can be operated under pressures ranging from UHV up to 10^{-5} Pa and at elevated pressures. Temperatures were measured using a K-type thermocouple that was spot-welded directly onto the sample. Gas pressures were measured by an ionization gauge that was calibrated for C_2H_4 . The clean Rh(111) surface was exposed to 1.3×10^{-8} Pa of ethylene at room temperature. During heating to 700 °C, the pressure of ethylene was increased from 1.3×10^{-8} Pa to 1.5×10^{-6} Pa in order to maintain growth irrespective of the increasing coverage of the active catalytic surface area. The temperature was held at 700 °C throughout the whole in situ STM observation of graphene growth. In this work, we show in situ STM images that were recorded in the phase where the pressure was 5.7×10^{-7} Pa.

2.3. In-situ scanning electron microscopy

In addition, in situ SEM observations were performed inside the chamber of a modified commercial ESEM (FEI Quantum 200). The vacuum system of the ESEM was modified and upgraded with oil-free pre-vacuum pumps. The instrument is equipped with a home-made laser heating stage, a gas supply unit (mass flow controllers from Bronkhorst), and a mass spectrometer (Pfeiffer OmniStar) for the analysis of the chamber atmosphere. Owing to the use of rubber O-rings for the sealing and the fact that the chamber cannot be baked out, the base pressure of the instrument is around 2×10^{-5} Pa, with a residual gas composition mostly comprising water, N_2 and O_2 . After each sample loading, the chamber was pumped out to around 10^{-3} Pa, purged with pure nitrogen, and pumped again to 10^{-3} Pa successively for several times. During the experiments, the microscope was operated at an acceleration voltage of 7.5 kV. Images were recorded by a large field detector during CVD growth and etching under high-vacuum and low-vacuum conditions, respectively. No influence of the electron beam on the growth and etching process could be observed. The imaged regions and their

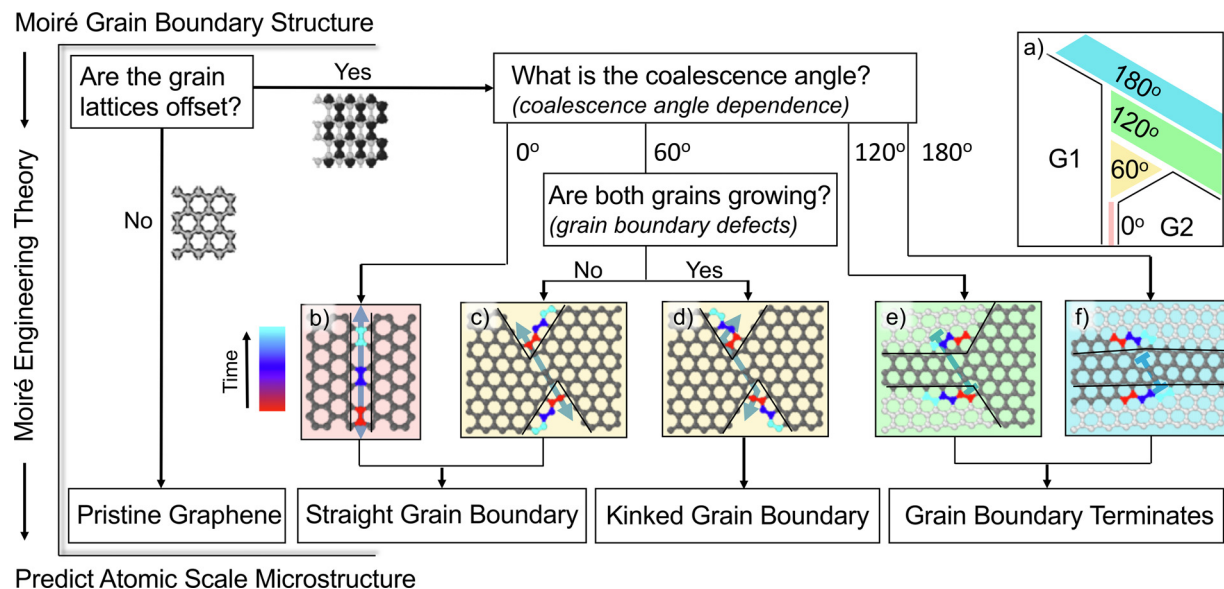


Fig. 1. The moiré metrology theory takes a moiré scale grain boundary structure and predicts the underlying atomic microstructure. The moiré metrology theory is presented as a decision tree that uses the lattice offset, coalescence angle, and grain growth to determine one of four grain boundary structures. (a) Four distinct coalescence angles give rise to the atomic structures shown in b-f. (b-f) The atomic mechanisms for the four coalescence angles (0° , 60° , 120° , 180°) for both octagon (top) and pentagon pair (bottom) coalescence fronts with a C-C distance of 1.42\AA . Atom color (red, blue, and cyan) is used to show the time-sequence of growth. (b) A straight grain boundary for a 0° coalescence angle. (c,d) The grain boundary structure for two different growth modes in the 60° coalescence case. This is discussed further in Figs. 2 and 3. (e,f) The faint hexagonal lattice shows the formation of pristine graphene after grain boundary termination. (For interpretation of the references to colour in this figure legend, the reader is referred to the web version of this article.)

respective surroundings showed similar behavior, as evidenced by changing the magnification or by moving the sample under the beam. Furthermore, no electron beam induced contamination was observed at elevated temperatures.

2.4. CVD Growth on rhodium

Under CVD growth conditions, the pressure is 6 orders of magnitude higher than the base pressure and constitutes mostly H_2 (99.9995% purity) and C_2H_4 (99.95% purity). Samples of sizes ranging from 4×4 to 5×5 mm are extracted from a 0.5 mm thick single-crystalline Rh (99.999% purity). Prior to all CVD growth experiments, the chamber of the ESEM was plasma cleaned. The crystals were annealed at 1100°C under a hydrogen flow of 10 sccm and oxygen flow 2 sccm at 46 Pa for more than 72 h inside the chamber to clean bulk dissolved carbon. The temperature was measured via a B-type thermocouple that was spot-welded onto the substrate, which simultaneously served to ground the sample. CVD growth was performed at 1000°C under 70 Pa ($\text{C}_2\text{H}_4:\text{H}_2 \approx 1:100$).

3. Atomistic origins of coalescence angle dependence

The moiré theory consists of two coupled atomistic models that reveal the mechanisms of nuclei coalesce. The models are presented for the simplified scenario of two isolated nuclei that coalesce, but also holds for the more complicated cases seen during growth and observed in supplementary videos 1 and 2.

The mechanisms governing nuclei coalescence on strongly interacting substrates are presented in Fig. 1 and are separated into three mechanisms. The first accounts for seamless coalescence and has been previously reported by Wang et al.[30], while the second and third are introduced here. The second mechanism predicts grain boundary propagation and termination for offset lattices as a function of the coalescence angle, which is readily observed from the moiré scale. The coalescence angle of graphene on strongly in-

teracting substrates is reduced to four possible angles due to the moiré interaction that aligns the nuclei to the substrate [35–37]. The continuum schematic in Fig. 1(a) shows each of the four coalescence angles (0° , 60° , 120° , 180°). The grain boundary structure is predicted for each coalescence angle by determining the carbon bonding at the coalescence front. The small number of coalescence angles makes it possible to exhaustively analyze the growth steps for each case by growing nuclei with carbon adatoms, dimers, or trimers as determined by Tettlow et al. [38]. For each coalescence angle the atomistic origins of grain boundary propagation and termination are shown in Fig. 1(b-f) for an anti-phase grain boundary that is formed between two offset grains. For 60° , 120° , and 180° coalescence angles, two unique terminations are presented. The two terminations are an octagon (top) and a pentagon pair (bottom).

Fig. 1 (b) details the formation of straight grain boundaries in a 0° coalescence angle. The zig-zag edges confine the carbon attachment to dimers that stitch together a straight grain boundary. Fig. 1(c,d) shows grain boundary formation in a 60° coalescence angle. A 60° coalescence angle provides less confinement than a 0° coalescence angle allowing the grain boundary to kink. The kinking is based on dimers forming rings with 4, 5, 6, 7, or 8 carbon atoms at the coalescence front. Four possible grain boundary structures are shown in the terminations of a 60° coalescence angle in Fig. 1(c,d), and are explored further in Section 4. Common among all the structures formed in a 60° coalescence angle is that they propagate a grain boundary due to carbon attachment being confined to only dimers.

In contrast to 0° and 60° coalescence angles, 120° and 180° coalescence angles both terminate grain boundaries. For a 120° coalescence angle, the boundary is only terminated at a pentagon pair termination (bottom of Fig. 1(e)) with a dimer (red) closing a heptagon. The grain boundary at an octagon termination grows one more unit until it has a pentagon pair termination and then terminates. A grain boundary with a 180° coalescence angle (Fig. 1(f)) terminates for both terminations. The pentagon pair is terminated

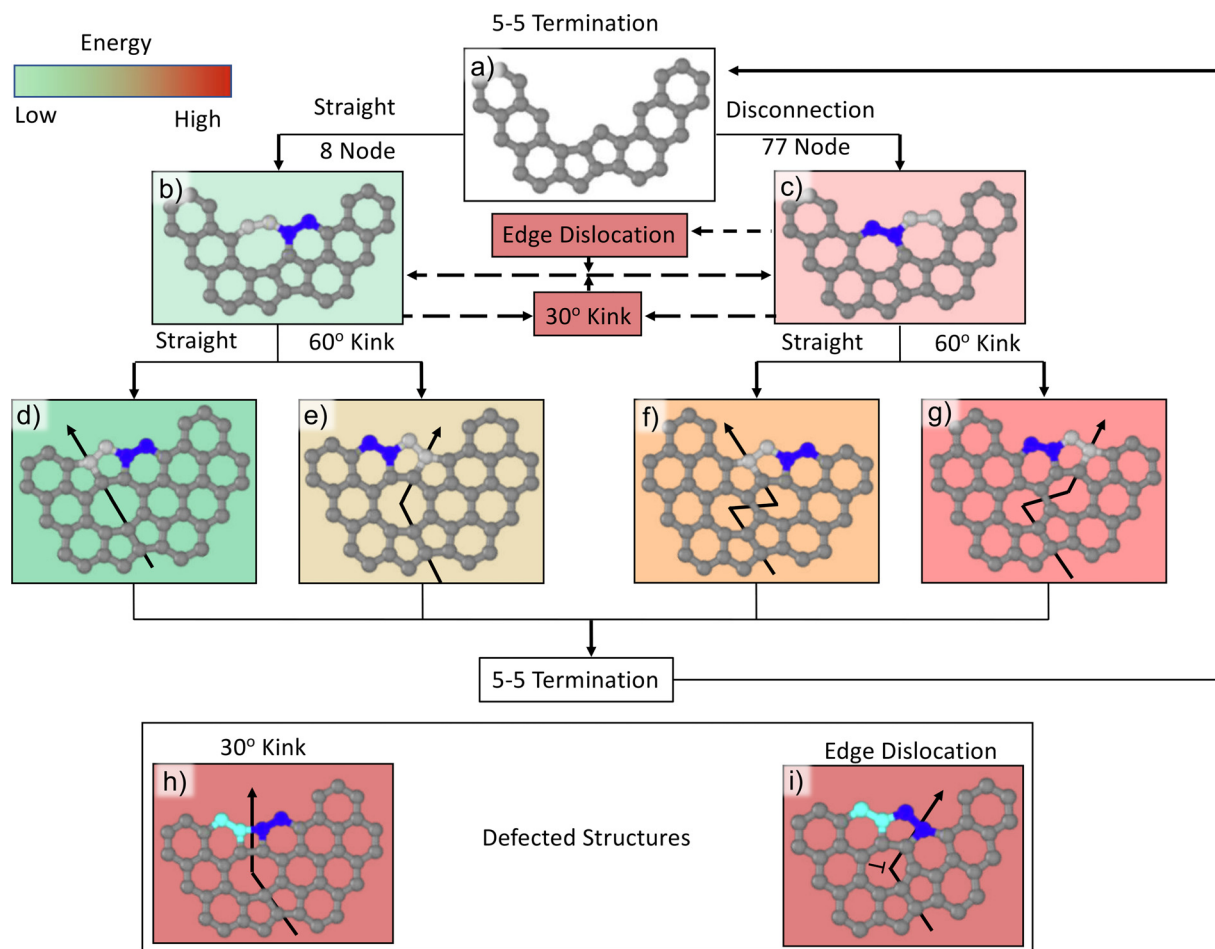


Fig. 2. Atomistic model of the structure and energetics of grain boundary formation for a 60° coalescence angle, where growth is shown with blue, gray, and teal carbon dimers with a C-C distance of 1.42 Å. (a) The growth cycle starts and ends with a pentagon-pair. (b,c) The first stage determines the central node, which forms either (b) a straight (octagon node) grain boundary due to a six carbon ring or (c) a disconnection (heptagon pair) in the grain boundary by forming a seven carbon ring. (d-g) The second stage determines the grain boundary direction (straight or 60° kink) of the grain boundary from the first stage. This is based on choosing between growing a hexagon on either the (e,g) left or (d,f) right grain. (h,i) Two high energy defected structures are associated with the model. (h) A 30° kink forms when the pentagon-pair dimer in the second stage forms a hexagon and four carbon ring instead. This can occur in both branches, although only the eight node structure is shown. (i) An edge dislocation forms during the first stage by forming a pentagon-hexagon structure instead of the gray heptagon in the disconnection structure. This requires a dimer (cyan) to attach to the blue heptagon. Both defect structures bypass the 5-5 termination and re-enter the process in the first stage, choosing between an 8 or 77 node. The flowchart is organized according to the relative energy of each pathway, where the relative energy is compared at each step (b-c or d-i) due to the different number of atoms. Green is the lowest, red the highest. The atomistic model is formulated from results of Monte Carlo simulations shown in the supplementary material. (For interpretation of the references to colour in this figure legend, the reader is referred to the web version of this article.)

by a dimer (teal) that closes a heptagon as in a 120° coalescence angle, but the octagon termination of the grain boundary at a 180° coalescence angle is terminated by a dimer (teal) that forms a single pentagon. In both 120° and 180° coalescence angles, the grain boundary terminates and subsequent growth does not contain a grain boundary. The pristine graphene grown after grain boundary termination is shown in Fig. 1(e,f) with a light gray hexagonal lattice.

The atomistic models for each coalescence angle predicts whether a grain boundary will propagate (0° and 60°) or terminate (120° and 180°) during coalescence. However, while the coalescence angle reveals the presence or absence of grain boundaries and the structure at the termination, it lacks information on the underlying complex atomic structure of propagating grain boundaries within a 60° coalescence angle. While the other three coalescence angles define a grain boundary topology, the 60° coalescence angle does not. Instead, it can grow on either grain to create arbitrary grain boundary structures. For this we establish a third coalescence mechanism that determines the structure of propagating grain boundaries in a 60° coalescence angle.

4. Atomistic origins of grain boundary defects

The third coalescence mechanism determines the structure of the propagating grain boundary in a 60° coalescence angle (Fig. 1(c,d)). The carbon attachment at the coalescence front determines which grain is growing and the grain boundary structure. The 60° coalescence angle is the only coalescence angle that propagates a non-straight grain boundary.

Whereas the growth steps for various coalescence angles were exhaustively studied analytically, the complexity of the 60° coalescence requires the development of an automated technique that can enumerate the events in a growth trajectory. The growth is simulated through a Monte Carlo (MC) model that calculates the chemical potential for all potential dimer attachments. The MC model is only constrained by the 60° coalescence topology, which fixes the degrees of freedom for carbon dimer attachment at each growth step. The MC results are synthesized into a cyclic model in Fig. 2, which presents the unique set of configurations with minimum chemical potential. The full MC results are in Appendix A and resemble previous theoretical works that de-

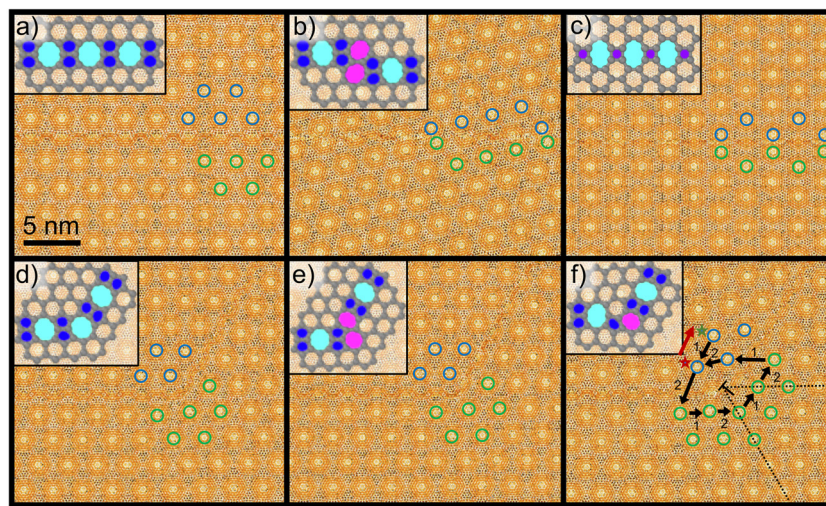


Fig. 3. Bond convolution images of isolated grain boundary structures from the atomistic model. The atomistic structures of each boundary that generated the bond convolutions are shown as insets with C-C spacing of 1.42 Å, where pentagons, heptagons, and octagons are filled with blue, magenta, and teal respectively. Teal and light green circles are used to emphasize the moiré pattern. (a) A straight 558 grain boundary shifts the moiré pattern across the boundary producing a 1D defect as seen in STM patterns. (b) A straight grain boundary with disconnections every three lattice vectors produces a moiré effect with the same periodicity to form 'half' moiré spots that are separated by large gaps along the boundary. (c) An armchair grain boundary from a 48 structure produces an anti-phase moiré pattern across the boundary. (d/e) A 60° kink with an octagon/pentagon-pair node produces a moiré defect that connects two straight 558 moiré boundaries (a) that are rotated 60° from each other. (f) A 60° kink with an edge dislocation as the central node produces a moiré pattern with a dislocation, highlighted by an edge dislocation symbol, Burgers circuit, and guiding lines to show the extra moiré spots caused by the dislocation in the graphene lattice. (For interpretation of the references to colour in this figure legend, the reader is referred to the web version of this article.)

termine optimal atomic structures of graphene grain boundaries [39,40].

The cyclic model presents the atomistic mechanisms of grain boundary propagation in a 60° coalescence angle. The cyclic model contains two steps that start and end with a pentagon pair termination in Fig. 2(a). The first step forms either an octagon (Fig. 2(b)) or a heptagon pair (Fig. 2(c)) between the pentagon pairs. The octagon step is the basis of a straight grain boundary, which is formed with a dimer that creates a hexagonal ring (blue) on the right grain. Alternatively, a dimer can close a heptagon ring (Fig. 2(c)), which forms a disconnection in the grain boundary [41,42].

Fig. 2 (d-g) details the second step, which determines the direction of the grain boundary based on the location of the pentagon pair. The pentagon pair forms either a straight grain boundary (Fig. 2(d,f)) or a 60° kink (Fig. 2(e,g)). The dimer that creates a hexagonal ring (blue) on the right grain (Fig. 2(d)) forms a straight grain boundary. Alternatively, the second step can create 60° kinks (Fig. 2(e,g)) when a dimer forms a hexagonal ring on the left grain. This is true for both initial steps of the cyclic model. The growth on the left grain is subsequently followed by the formation of a pentagon pair. The pentagon pair cycles back to the beginning of the model to traverse the decision tree again.

In addition to the four low-energy structures, two defected structures can form. These two structures have relatively high energies and occur infrequently. The first kinks the grain boundary by 30° (Fig. 2(h)), forming a hexagon on both the left (teal) and right (blue) grains that bisect the 60° opening. The hexagons bond to create a high energy four member ring. The 30° kink comes out of both branches and replaces the second step that forms the pentagon-pair. The cycle continues by growing either an octagon or heptagon-pair node.

The second defected structure forms an edge dislocation and comes out of only the disconnection branch (Fig. 2(i)). The edge dislocation alters the heptagon-pair that is formed in Fig. 2(c). The edge dislocation is formed through a two step hexagon then pentagon growth instead of forming the second (gray) heptagon. The structure replaces the pentagon pair as the entrance to the cyclic

model. The dislocation formation mechanism is based on the addition of a single dimer during the growth process to add a half-plane of atoms. This is distinct from the common interpretation that dislocations form as topologically necessary dislocation between two misoriented nuclei.

The six structures the cyclic model identifies (Fig. 2(d-i)) are sorted according to their formation energies and are the grain boundary building blocks [43,44]. The straight grain boundary is the low energy structure that would form if graphene was synthesized without any substrate interaction at zero Kelvin. However, substrate interaction and temperature push the grain boundary structure to higher in-plane energies. We show how the substrate interaction affects the grain boundary structure in Appendix A.

5. Bridging simulation and experiment with bond convolution

The moiré theory is completed by promoting the atomistic models to the moiré scale. While the coalescence angles are naturally visible at the moiré scale, the cyclic model needs to be brought to the moiré scale through simulation. We promote the atomic scale mechanisms of the cyclic model to the moiré scale through bond-convolution, a moiré simulation technique that mimics the electron density from STM [12]. The six structures identified in Fig. 2 are separated into three straight grain boundaries and three with 60° kinks.

The straight grain boundaries are (a) an anti-phase 558 grain boundary, (b) a 558 grain boundary with disconnections every three lattice vectors, and (c) a 48 armchair grain boundary. The 558 boundary promotes the atomic offset to create an offset in the moiré lattice shown in the larger spacing between blue/green circles as opposed to the blue-blue or green-green spacing in Fig. 3(a). The atomic scale disconnections cause the offset between the moiré patterns to shift every three moiré spots, the same periodicity as the atomic scale disconnections. The disconnection is identified at the moiré scale in Fig. 3(b) by the proximity of moiré spots, where a pair of close spots is followed by a gap between subsequent spots. Finally, an array of 30° kinks in Fig. 3(c) creates

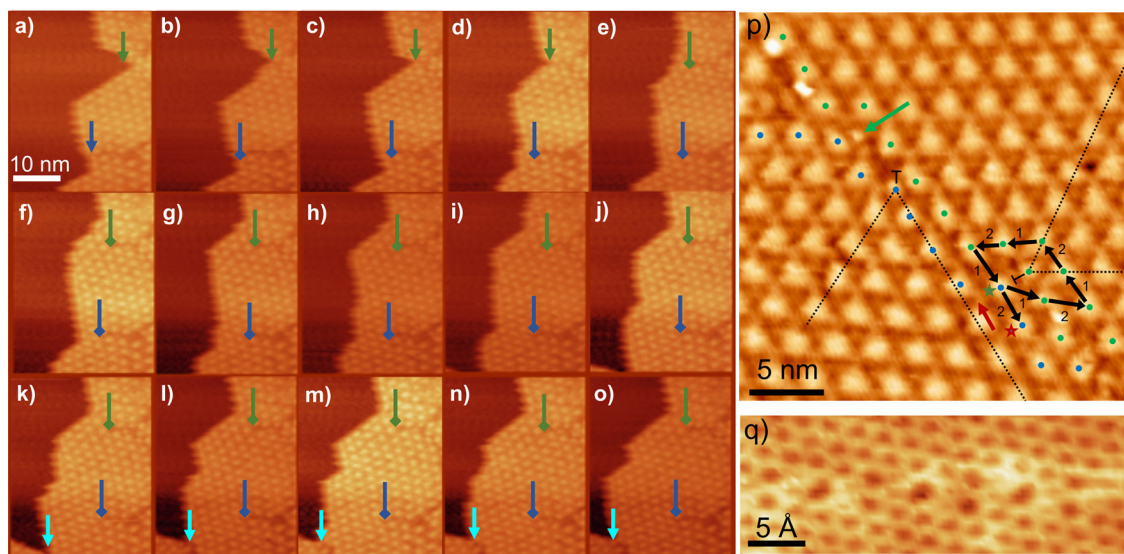


Fig. 4. Moiré scale in-operando STM micrographs. (a-o) Nanoscale moiré (yellow spots) time series ($dt=26.2$ seconds) of graphene coalescence on Rhodium. Three grain boundaries, appearing as 1D defects in the moiré lattice, are observed during growth and show the dependence of grain boundary propagation on coalescence angle. Arrows highlight the coalescence front of the grain boundaries over time. The arrowhead changes to a diamond when the grain boundary stops propagating. (p) Moiré STM image of a CVD graphene grain boundary with moiré metrology post-processing to reveal the structure of graphene grain boundaries. Blue/green circles are superimposed on the moiré spots adjacent to the boundary of the left/right grains. A green arrow is used to point to a 'half' moiré spot from a disconnection associated with the right grain. Two edge dislocations are highlighted with an edge dislocation symbol, a Burgers circuit, and guide lines to show the extra moiré spots. (q) Atomic scale STM image of a region of the boundary close to the 'half' moiré spot associated with the right grain. The atomic scale structure has alternating octagon and disconnection nodes. (For interpretation of the references to colour in this figure legend, the reader is referred to the web version of this article.)

a 48 armchair boundary recognized at the moiré scale by the rotation of the lattices.

The three grain boundaries with 60° kinks also promote the atomistic details to the moiré scale. In each case, the 60° kink is brought to the moiré scale. For the octagon and heptagon node 60° kinks in Fig. 3(d,e), the offset is rotated without any additional defect. Even though the two kinks have different core structures, the two are identical at the moiré scale because their long-range strain fields are identical. However, the strain field from the core with an edge dislocation in Fig. 3(f) causes a dislocation to appear in the moiré pattern, which is observed in the additional moiré rows in the bottom (green) grain.

All of the boundaries promote a signature of their atomistic structure to the moiré scale. However, the moiré promotion imposes a limit on the resolution. For straight grain boundaries, the structure must be repeated over the length of a moiré period, while for the 60° case kinks must be isolated from other defects by more than a moiré wavelength. The promoted features in experimental moiré images are therefore a lower bound of the number of topological defects present in STM images. However, the lower energy of a straight grain boundary increases its frequency mitigating concerns over the resolution.

The moiré structure predicted by the atomistic models is compared to in-operando STM micrographs in Fig. 4. Grain boundaries are observed as 1D defects in the triangular moiré lattice. The time series in Fig. 4(a-o) verify that coalescence angles of 60° will propagate and 120° and 180° will terminate grain boundaries, while Fig. 4(p,q) verify the atomic structures of the cyclic model.

The time series contains three grain boundaries each labelled with a colored arrow, which changes to a diamond arrow when the front no longer propagates. The green arrow, located at the top of Fig. 4(a), identifies a grain boundary barely visible at the right edge of the frame. The grain boundary has a 60° coalescence angle for Fig. 4(a-e) before it transforms into a 120° opening. In Fig. 4(e), the grain boundary trajectory verifies that a 60° opening allows for a grain boundary to propagate. From Fig. 4(e) onwards, the graphene continues to grow at the green grain boundary with a 120° coales-

cence angle. But, there are no defects in the moiré lattice signifying a terminated grain boundary at the 120° coalescence angle. A second grain boundary (teal arrow) in Fig. 4(k-o) confirms that grain boundaries in a 60° coalescence angle propagate.

A third grain boundary is highlighted with a blue arrow. A grain boundary can be traced from the blue arrow to the right edge of the micrographs. The blue arrow in Fig. 4(a) is at a 180° opening, slightly above a 120° opening, and a row of moiré spots are growing from above. The grain boundary does not propagate. In Fig. 4(o), there are six moiré spots in front of the grain boundary, none of which are defected.

These three grain boundaries support the predictions of our mechanistic model. Grain boundaries can either propagate (0° and 60°) or terminate (120° and 180°) during coalescence. This is in agreement with experimental images that show poly-crystalline graphene with grains partially surrounded by grain boundaries coming from the termination of grain boundaries as the coalescence angle transitions from 60° to 120° [45].

Furthermore, a sample analysis of the moiré theory is applied to an STM grain boundary in Fig. 4(p). The moiré metrology technique can identify numerous 60° kinks, a region of disconnections, and a pair of edge dislocations. The 60° kinks are identified using the moiré spots of each grain. The disconnection is identified by a moiré spot that is closer than the moiré spacing identified by the green arrow in Fig. 4(p). The disconnections are verified by atomic scale STM in Fig. 4(q) to reveal a set of disconnections underlying the disconnection feature in Fig. 4(p). Finally, two edge dislocations are identified through Burgers circuits that show the extra moiré spots in the lattice corresponding to Fig. 3(f). In combination, the time series and sample analysis confirm the ability of atomistic mechanistic models to bridge the scale gap and provide atomic scale details from the moiré scale.

6. Discussion

Each of the two proposed mechanisms in our moiré theory can be used to engineer a desired grain boundary structure. The first

mechanism determines the presence or absence of grain boundaries that impart local strain to a graphene sample. A high nucleation density can be designed using nuclei that coalesce with predominantly 0° and 60° coalescence angles, where the specific atomic structure can be tuned using the cyclic model in Fig. 2. Alternatively, graphene with very few defects could be synthesized. Intuitively, a low nucleation density is associated with a low number of defects, but our model shows how large isolated nuclei can lead to large grain boundaries forming as two nuclei are stitched together with a 60° coalescence angle. Instead, our model suggests that a more moderate nucleation density or non-hexagonal flakes would prevent large grain boundaries to form as coalescence angles quickly become 120° or 180° . The non-intuitive predictions of our mechanistic model call for more simulations using the identified mechanisms to predict the ideal growth conditions for specific grain boundary structures.

The second proposed mechanism facilitates both understanding and observation of atomic scale defects during growth without needing an atomic resolution microscopy technique. The technique can identify edge dislocations, disconnections, and 60° kinks like in sample analysis of Fig. 4(p) during growth. We envision that strain mapping and dislocation analysis software for STM micrographs could be utilized to automatically identify the formation of these topological features [46]. This enables decision making during growth to achieve a particular grain boundary structure by either removing the defect through an etch-regrowth step or electing to keep grain boundaries and their defects (see Appendix C). Moreover, the cyclic model is the foundation of mechanistic simulations that can predict the structure of a grain boundary for a given substrate interaction as a way to rationally design the grain boundary structure of graphene.

7. Conclusion

In conclusion, we have proposed a moiré theory which extends the capability of in-operando microscopy by bridging the observable moiré pattern to atomic scale features. The moiré theory is based on atomistic models that are promoted to the moiré scale through simulation. We develop this theory through studying the coalescence of graphene nuclei during synthesis and introduce two novel mechanistic models that govern coalescence. The mechanistic models for the first time show how edge dislocations, disconnections, and grain boundaries form from the attachment of individual dimers. We end by proposing how this approach enables both new insight into graphene growth and decision making of synthesis conditions due to information of grain boundary structure through during growth.

Data Availability

The raw/processed data required to reproduce these findings cannot be shared at this time due to technical or time limitations.

Declaration of Competing Interest

The authors declare that they have no known competing financial interests or personal relationships that could have appeared to influence the work reported in this paper.

CRediT authorship contribution statement

Emil Annevelink: Conceptualization, Methodology, Software, Formal analysis, Investigation, Writing – original draft, Visualization. **Zhu-Jun Wang:** Investigation, Writing – review & editing. **Guocai Dong:** Investigation. **Harley T. Johnson:** Conceptualization, Writing – review & editing, Supervision, Funding acquisition.

Pascal Pochet: Conceptualization, Writing – review & editing, Supervision, Project administration, Funding acquisition.

Acknowledgements

EJA and HTJ acknowledge support from the Army Research Office (ARO) under grant W911NF-17-1-0544. HTJ acknowledges additional support from NSF grant CMMI 18-25300. PP acknowledges partial support from The French National Research Agency (ANR-14-OHRI-0004). Additionally, we acknowledge helpful conversations with Prof. Elif Ertekin, Dr. Johann Coraux, Dr. Muriel Sicot.

Appendix A. Monte Carlo Graphene Nuclei Coalescence

The growth mechanism in a 60° coalescence angle is addressed by creating a Monte Carlo (MC) coalescence simulation using a carbon dimer growth mechanism. The dimers bond to the graphene edges to form carbon rings of four, five, six, seven, or eight atoms. The simulation can be understood as the competition of two thermodynamic terms: the in-plane graphene bonding E_{gr} and out-of-plane substrate bonding $E_{sub}(s)$. The carbon-carbon bonding energy E_{gr} favors hexagonal carbon rings, while the substrate bonding $E_{sub}(s)$ adds a spatially varying term that follows the periodicity of the moiré, shown in Fig. A.5. The interplay between the two thermodynamic terms determines the structure of the boundary. The graphene energy is modeled using a reactive potential (REAX) [47,48] fitted to hydrocarbons [34] that accounts for the edge nature of graphene, while the substrate energy is modeled using a Lennard-Jones (LJ) potential.

A1. Dimer growth on zig-zag edge

The substrate interaction is tested by growing a triangular graphene flake row-by-row. Each row is nucleated with a trimer, grown along a zig-zag edge with dimers, and terminated with two more trimers to make a perfect triangular flake. Fig. A.5(a) isolates one step of the growth, which shows a triangular graphene flake on top of a triangular substrate (black). The substrate mimics the top layer of a (111) rhodium surface with a triangular lattice.

The row-by-row growth shows the moiré periodicity of the dimer growth. We do that by showing the excess energy of dimer growth in Fig. A.5(b). The excess energy is found by subtracting the cohesive energy associated with carbon sp₂ bonding in-plane. The excess energy is plotted for 28 rows of carbon starting with a triangle that has an edge length of three moiré spots. The excess energy shows the hexagonal moiré symmetry arising from the 6 (graphene) on 3 (substrate) interaction.

The substrate interaction is used to simulate bonding at the edge of a high-interacting substrate. We tune the Lennard-Jones

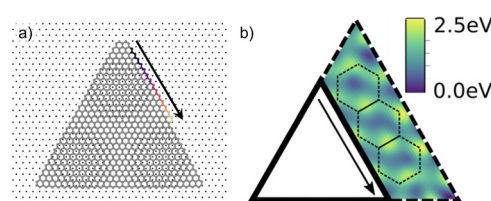


Fig. A1. Test of the Lennard-Jones substrate interaction. (a) Atomic scale depiction of a triangular graphene flake on a triangular substrate. The top right edge grows dimer by dimer following the black arrow, where the dimers are colored from dark to light to showcase the order of dimer growth. (b) Energy map of the energy contribution from a Lennard-Jones interface potential for a dimer growth in (a). The spatial variation of the interface energy is based on the stacking, which is topologically related to the hexagonal dislocation network (dotted lines) of a 6 (graphene) on 3 (rhodium) interface.

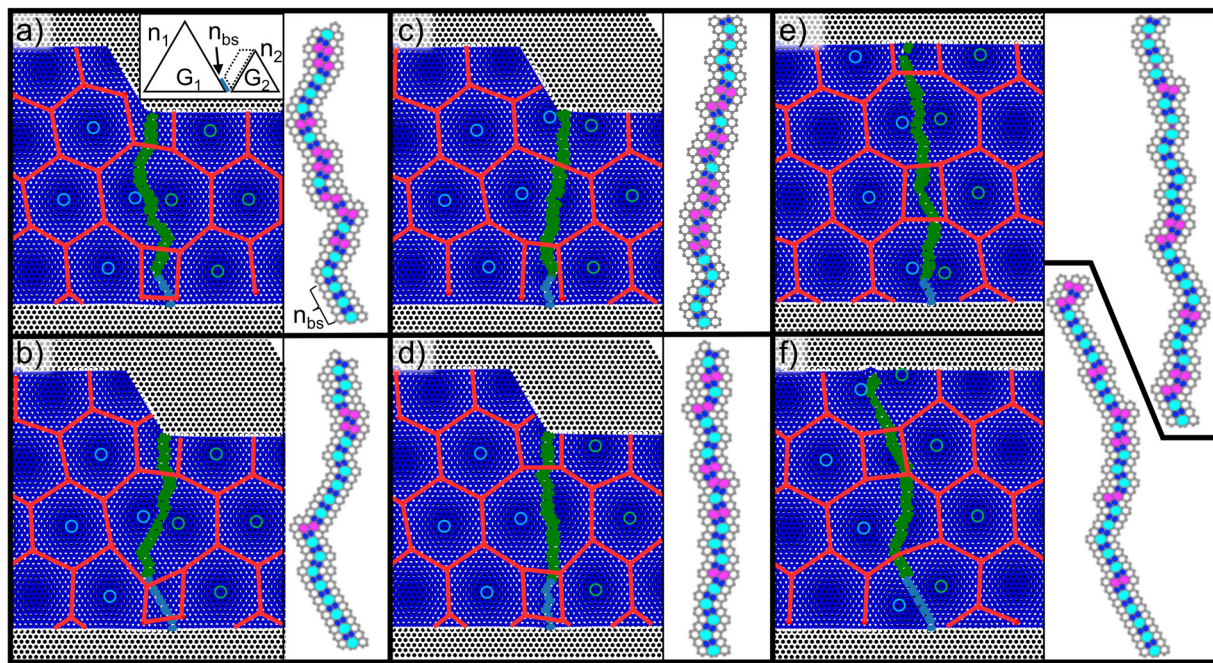


Fig. A2. Moiré and atomic scale images of OK Monte Carlo grain boundaries for six different initial conditions. The inset in (a) defines the simulation parameters that describe two triangular grains with sizes n_1 , n_2 and attached with an initial boundary of length n_{bs} resulting from initial growth (light blue). The moiré images are atomic convolution images of the coalesced graphene nuclei (blue) on a triangular lattice (black) with the same lattice constant as Ruthenium ($a_{sub} = 2.69 \text{ \AA}$). The grain boundary is highlighted in green and the moiré pattern is highlighted with both a hexagonal dislocation pattern superimposed in red and circles (teal/light green for left/right nuclei) to demonstrate the moiré spots. The atomic scale images isolate the structure of the boundary, where non-hexagonal rings are colored with violet (4 carbon ring), blue (5 carbon ring), pink (7 carbon ring), and cyan (8 carbon ring). The initial conditions are given according to the size of initial nuclei given by number of lattice sites along the nuclei edges (moiré wavelengths) and the length and direction (zig-zag or armchair) of the initial boundary given with respect to the size of the graphene lattice. (a) $n_1 : 55(4)$, $n_2 : 41(3)$, $n_{bs} : 4zz$ (b) $n_1 : 55(4)$, $n_2 : 41(3)$, $n_{bs} : 9zz$ (c) $n_1 : 55(4)$, $n_2 : 41(3)$, $n_{bs} : 4ac$ (d) $n_1 : 55(4)$, $n_2 : 41(3)$, $n_{bs} : 8ac$ (e) $n_1 : 55(4)$, $n_2 : 55(4)$, $n_{bs} : 3zz$ (f) $n_1 : 55(4)$, $n_2 : 55(4)$, $n_{bs} : 9zz$. (For interpretation of the references to colour in this figure legend, the reader is referred to the web version of this article.)

parameters such to make the excess energy range high enough to influence the dimer addition. We chose a range of 2.5eV because it was comparable in magnitude to graphene cohesive energy of 7eV/atom.

A2. Monte carlo grain boundaries

Grain boundary trajectories are shown in Fig. A6 for six initial conditions of varying nuclei with sizes n_1 , n_2 and initial grain boundary length n_{bs} . The simulation is initialized with two offset grains shown in the inset of Fig. A6(a). After initialization, there are no constraints on the carbon atoms, where the grain location and orientation are maintained by the substrate interaction. The grain boundary trajectories are shown at both the moiré and atomic scale. The moiré scale highlights how the grain boundary trajectory is shaped by the periodic variation of stacking. The atomic convolution moiré pattern of the graphene (blue) on the substrate (black) and the interlayer dislocation network (red) shows the spatial variation of the stacking. The grain boundary is highlighted as well, where the initial grain boundary is light blue and the MC grain boundary is green. The atomic scale structure is shown through ball and stick schematics, where rings of different 4, 5, 7, and 8 carbon atoms are highlighted with purple, blue, magenta, and cyan respectively.

All the grain boundary trajectories in Fig. A6 are in the armchair direction of the moiré dislocation network. This is due to the higher substrate interaction since removing the substrate interaction term produces grain boundaries in the zig-zag direction. This points to a route for design of the grain boundary trajectory based on the strength and periodicity of the moiré interaction.

The difference between zig-zag and armchair directions is seen by comparing Fig. A6(a,b) to S.A6(c,d). In Fig. A6(a,b), the initial

boundary (light blue) is along the zig-zag edge of grain 1, however once the MC algorithm takes over growth, the grain boundary alternates directions to give an overall direction in the armchair direction. However, in Fig. A6(c,d), the initial grain boundaries are in the armchair direction and the MC growth does not alter the overall direction.

This method shows the potential for the moiré to design the structure of graphene grain boundaries. However, neither the REAX nor LJ potentials model the interactions very accurately. An ab-initio parameterization of both energy terms to accurately account for the unique edge and chemical effects of this problem would allow for accurate modeling and facilitate design of moiré topologies that produce desired grain boundaries.

We combine the dislocations network with the atomic images and observe that dimers preferentially form hexagonal rings that are further away from a dislocation line. This is analogous to the predictable conclusion that carbon rings with lower graphene binding energies (six carbon rings) and lower substrate binding energies (far from dislocations) are chosen by the OK MC model. This leads to a general trend that the grain boundaries intersect perpendicular to the dislocation lines.

Appendix B. SEM Pressure Bridging Analysis

We compare the orientation of graphene nuclei on rhodium at different growth conditions to show the universality of the coalescence model under different graphene pressures. Here we briefly show a comparison of scanning electron microscopy (SEM) and scanning tunneling microscopy (STM) that are taken at 200 Pa and UHV conditions respectively. A more in depth comparison of the pressure bridging is shown in [30]. By comparing the two growth conditions, we can show that the proposed mechanisms are gen-

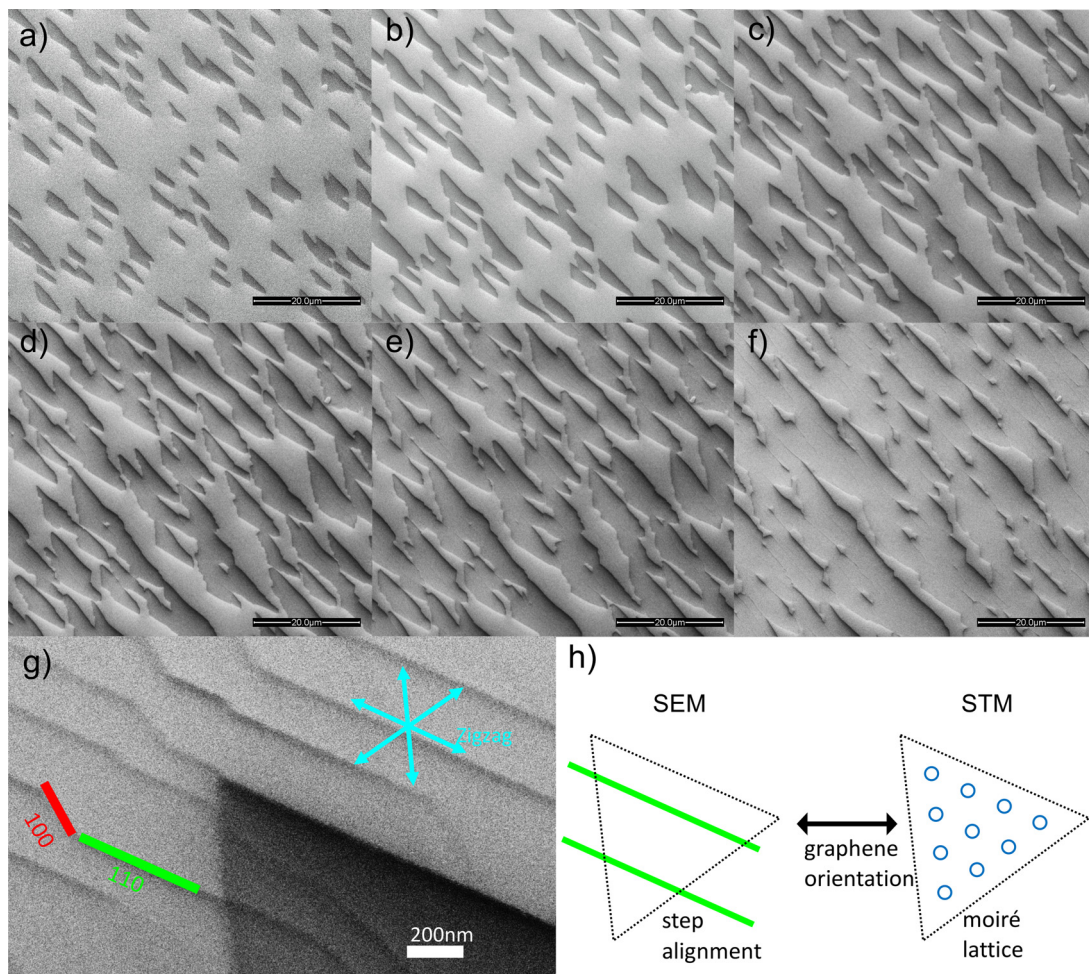


Fig. B1. In-operando SEM growth. (a-f) In-operando SEM of six micrographs of graphene on rhodium, where the scale bar is 20 microns and the graphene is the darker contrast. (g) Tip of a graphene flake (dark), where the teal arrows are parallel to the zig-zag directions, shown in teal on top of a rhodium substrate with (100) and (110) step edges shown in red and green respectively. (h) Comparison of SEM and STM micrographs to show the alignment of graphene on Rhodium. (For interpretation of the references to colour in this figure legend, the reader is referred to the web version of this article.)

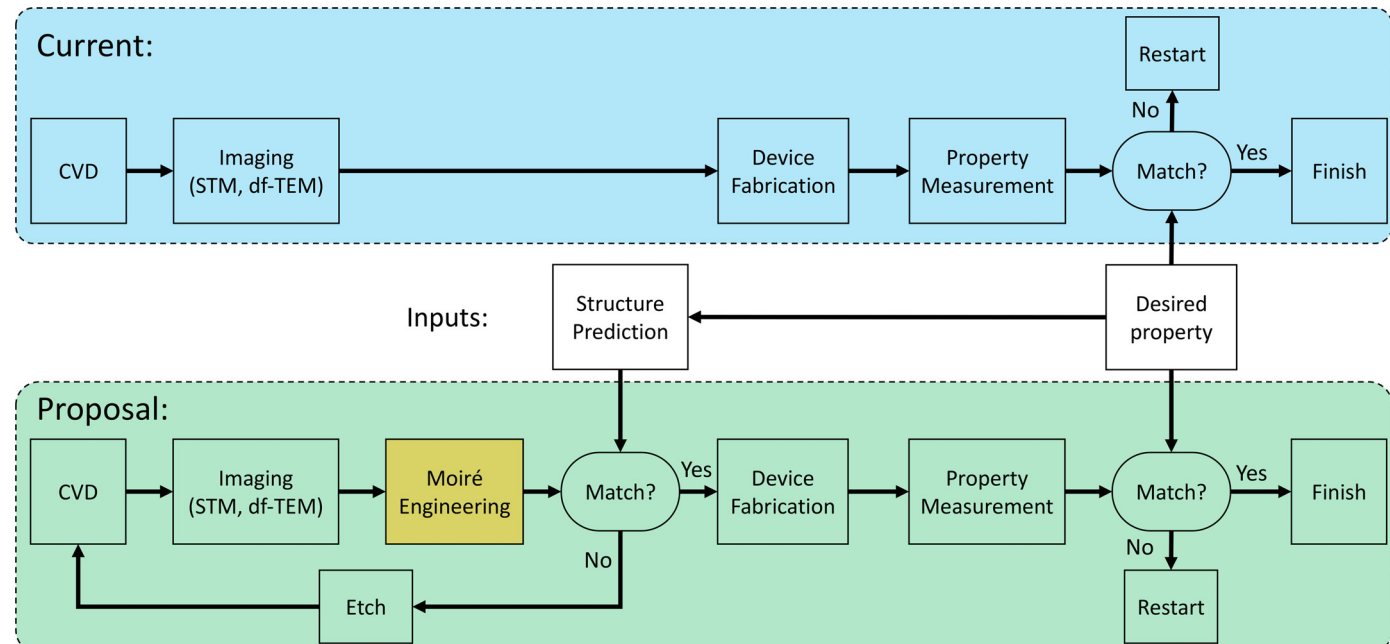


Fig. C1. Comparison of current synthesis methods with the addition of moiré metrology. Moiré metrology adds the ability to extract the structure of a grain boundary from in-operando microscopy to check if it matches a desired structure. If so, the growth progresses to create a device. If not, the sample can be etched in-situ.

eral and apply to more typical CVD conditions that are observed during SEM. Fig. B.7 contains a growth sequence of SEM data which we compare to the STM data in the main text. Fig. B.7(a-f) show the growth and coalescence of many graphene nuclei, which have dark contrast. The nuclei from SEM and STM are compared by connecting the orientation of the flakes to the substrate, where the orientation in SEM is given by the step orientation and the STM from the moiré lattice. In Fig. B.7(g), the step orientations are (100) in red and (110) in green. These orientations are compared to the coalescence angle to show that the zig-zag edges are along the (110) direction of the substrate. Fig. B.7(h) shows the agreement between coalescence fronts for the SEM and STM images. The orientation of the SEM zig-zag edges are given by the step directions, while the orientation of the STM ziz-zag edges are given by the moiré.

Appendix C. Moiré metrology during growth

The moiré metrology method is able to understand the atomic structure from the moiré scale. Although this method could be used anytime, we believe it is especially useful during growth using in-operando STM images. The proposed method would add flexibility to the current growth process by enabling decision making from in-operando microscopy of the structure. The grown structure is compared to a predicted structure for a given device. If the structures match, the growth would continue to measure the structure through device fabrication. However, if the structure does not match, the growth can be reversed by changing the precursor concentrations to etch graphene and restart growth.

Supplementary material

Supplementary material associated with this article can be found, in the online version, at doi:[10.1016/j.actamat.2021.117156](https://doi.org/10.1016/j.actamat.2021.117156)

References

- [1] Y. Wei, J. Wu, H. Yin, X. Shi, R. Yang, M. Dresselhaus, The nature of strength enhancement and weakening by pentagon-heptagon defects in graphene, *Nat Mater* 11 (9) (2012) 759–763, doi:[10.1038/nmat3370](https://doi.org/10.1038/nmat3370).
- [2] H. Qin, Y. Sun, J.Z. Liu, M. Li, Y. Liu, Negative poisson's ratio in rippled graphene, *Nanoscale* 9 (2017) 4135–4142, doi:[10.1039/C6NR07911C](https://doi.org/10.1039/C6NR07911C).
- [3] I. Leven, D. Krepel, O. Shemesh, O. Hod, Robust superlubricity in graphene/h-BN heterojunctions, *J Phys Chem Lett* 4 (1) (2013) 115–120, doi:[10.1021/jz301758c](https://doi.org/10.1021/jz301758c). PMID: 26291222.
- [4] G.S. Jung, J. Yeo, Z. Tian, Z. Qin, M.J. Buehler, Unusually low and density-insensitive thermal conductivity of three-dimensional gyroid graphene, *Nanoscale* 9 (2017) 13477–13484, doi:[10.1039/C7NR04455K](https://doi.org/10.1039/C7NR04455K).
- [5] O.V. Yazyev, S.G. Louie, Electronic transport in polycrystalline graphene, *Nat Mater* 9 (10) (2010) 806–809, doi:[10.1038/nmat2830](https://doi.org/10.1038/nmat2830).
- [6] Y. Cao, V. Fatemi, S. Fang, K. Watanabe, T. Taniguchi, E. Kaxiras, P. Jarillo-Herrero, Unconventional superconductivity in magic-angle graphene superlattices, *Nature* 556 (7699) (2018) 43–50, doi:[10.1038/nature26160](https://doi.org/10.1038/nature26160).
- [7] Y. Hao, M.S. Bharathi, L. Wang, Y. Liu, H. Chen, S. Nie, X. Wang, H. Chou, C. Tan, B. Fallahazad, H. Ramanarayanan, C.W. Magnuson, E. Tutuc, B.I. Yakobson, K.F. McCarty, Y.-W. Zhang, P. Kim, J. Hone, L. Colombo, R.S. Ruoff, et al., The role of surface oxygen in the growth of large single-crystal graphene on copper, *Science* 342 (6159) (2013) 720–723, doi:[10.1126/science.1243879](https://doi.org/10.1126/science.1243879). <https://science.sciencemag.org/content/342/6159/720.full.pdf>
- [8] Y. Hao, L. Wang, Y. Liu, H. Chen, X. Wang, C. Tan, S. Nie, J.W. Suk, T. Jiang, T. Liang, J. Xiao, W. Ye, C.R. Dean, B.I. Yakobson, K.F. McCarty, P. Kim, J. Hone, L. Colombo, R.S. Ruoff, Oxygen-activated growth and bandgap tunability of large single-crystal bilayer graphene, *Nat Nanotechnol* 11 (5) (2016) 426–431, doi:[10.1038/nnano.2015.322](https://doi.org/10.1038/nnano.2015.322).
- [9] X. Xu, Z. Zhang, L. Qiu, J. Zhuang, L. Zhang, H. Wang, C. Liao, H. Song, R. Qiao, P. Gao, Z. Hu, L. Liao, Z. Liao, D. Yu, E. Wang, F. Ding, H. Peng, K. Liu, Ultrafast growth of single-crystal graphene assisted by a continuous oxygen supply, *Nat Nanotechnol* 11 (11) (2016) 930–935, doi:[10.1038/nnano.2016.132](https://doi.org/10.1038/nnano.2016.132).
- [10] I. Vlassiouk, M. Regmi, P. Fulvio, S. Dai, P. Datskos, G. Eres, S. Smirnov, Role of hydrogen in chemical vapor deposition growth of large single-crystal graphene, *ACS Nano* 5 (7) (2011) 6069–6076.
- [11] Y. Zhang, L. Zhang, C. Zhou, Review of chemical vapor deposition of graphene and related applications, *Acc. Chem. Res.* 46 (10) (2013) 2329–2339, doi:[10.1021/ar300203n](https://doi.org/10.1021/ar300203n). PMID: 2348016.
- [12] P. Pochet, B.C. McGuigan, J. Coraux, H.T. Johnson, Toward moiré engineering in 2d materials via dislocation theory, *Applied Materials Today* 9 (2017) 240–250, doi:[10.1016/j.apmt.2017.07.007](https://doi.org/10.1016/j.apmt.2017.07.007).
- [13] E. Annevelink, H.T. Johnson, E. Ertekin, Topologically derived dislocation theory for twist and stretch moiré superlattices in bilayer graphene, *Phys. Rev. B* 102 (2020) 184107, doi:[10.1103/PhysRevB.102.184107](https://doi.org/10.1103/PhysRevB.102.184107).
- [14] S. Terada, T. Yokoyama, N. Saito, Y. Okamoto, T. Ohta, Growth and moiré superstructure of palladium films on ni(111) studied by STM, *Surf Sci* 433–435 (1999) 657–660, doi:[10.1016/S0039-6028\(99\)00138-7](https://doi.org/10.1016/S0039-6028(99)00138-7).
- [15] K. Kobayashi, Moiré pattern in scanning tunneling microscopy of monolayer graphite, *Phys. Rev. B* 50 (1994) 4749–4755, doi:[10.1103/PhysRevB.50.4749](https://doi.org/10.1103/PhysRevB.50.4749).
- [16] J.S. Alden, A.W. Tsen, P.Y. Huang, R. Hovden, L. Brown, J. Park, D.A. Muller, P.L. McEuen, et al., Strain solitons and topological defects in bilayer graphene, *Proceedings of the National Academy of Sciences* 110 (28) (2013) 11256–11260, doi:[10.1073/pnas.1309394110](https://doi.org/10.1073/pnas.1309394110). <https://www.pnas.org/content/110/28/11256.full.pdf>
- [17] K. Hermann, Periodic overlayers and moiré patterns: theoretical studies of geometric properties, *J. Phys.: Condens. Matter* 24 (31) (2012) 314210, doi:[10.1088/0953-8984/24/31/314210](https://doi.org/10.1088/0953-8984/24/31/314210).
- [18] F. Ke, X.-L. Yin, N. Tong, C.-F. Lin, N. Liu, R.-G. Zhao, L. Fu, Z.-F. Liu, Z.-H. Hu, Moiré patterns and step edges on few-layer graphene grown on nickel films, *Chin. Phys. B* 23 (11) (2014) 116801, doi:[10.1088/1674-1056/23/11/116801](https://doi.org/10.1088/1674-1056/23/11/116801).
- [19] M. Smirman, D. Taha, A.K. Singh, Z.-F. Huang, K.R. Elder, Influence of misorientation on graphene moiré patterns, *Phys. Rev. B* 95 (2017) 085407, doi:[10.1103/PhysRevB.95.085407](https://doi.org/10.1103/PhysRevB.95.085407).
- [20] B.C. McGuigan, P. Pochet, H.T. Johnson, Critical thickness for interface misfit dislocation formation in two-dimensional materials, *Phys. Rev. B* 93 (2016) 214103, doi:[10.1103/PhysRevB.93.214103](https://doi.org/10.1103/PhysRevB.93.214103).
- [21] I. Vlassiouk, S. Smirnov, M. Regmi, S.P. Surwade, N. Srivastava, R. Feenstra, G. Eres, C. Parish, N. Lavrik, P. Datskos, S. Dai, P. Fulvio, Graphene nucleation density on copper: fundamental role of background pressure, *The Journal of Physical Chemistry C* 117 (37) (2013) 18919–18926, doi:[10.1021/jp407648](https://doi.org/10.1021/jp407648).
- [22] K. Kim, Z. Lee, W. Regan, C. Kisielowski, M.F. Crommie, A. Zettl, Grain boundary mapping in polycrystalline graphene, *ACS Nano* 5 (3) (2011) 2142–2146, doi:[10.1021/nn1033423](https://doi.org/10.1021/nn1033423).
- [23] P.Y. Huang, C.S. Ruiz-Vargas, A.M. van der Zande, W.S. Whitney, M.P. Levent-dorf, J.W. Kevek, S. Garg, J.S. Alden, C.J. Hustedt, Y. Zhu, J. Park, P.L. McEuen, D.A. Muller, et al., Grains and grain boundaries in single-layer graphene atomic patchwork quilts, *Nature* 469 (7330) (2011) 389–392, doi:[10.1038/nature09718](https://doi.org/10.1038/nature09718).
- [24] S. Marchini, S. Günther, J. Winterlin, Scanning tunneling microscopy of graphene on ru(0001), *Phys. Rev. B* 76 (2007) 075429, doi:[10.1103/PhysRevB.76.075429](https://doi.org/10.1103/PhysRevB.76.075429).
- [25] S. Yin, X. Zhang, C. Xu, Y. Wang, Y. Wang, P. Li, H. Sun, M. Wang, Y. Xia, C.-T. Lin, P. Zhao, H. Wang, Chemical vapor deposition growth of scalable monolayer polycrystalline graphene films with millimeter-sized domains, *Mater Lett* 215 (2018) 259–262, doi:[10.1016/j.matlet.2017.12.121](https://doi.org/10.1016/j.matlet.2017.12.121). <http://www.sciencedirect.com/science/article/pii/S0167577X17318888>
- [26] P.W. Sutter, J.-I. Fleige, E.A. Sutter, Epitaxial graphene on ruthenium, *Nat Mater* 7 (5) (2008) 406–411, doi:[10.1038/nmat2166](https://doi.org/10.1038/nmat2166).
- [27] G. Odahara, S. Otani, C. Oshima, M. Suzuki, T. Yasue, T. Koshikawa, In-situ observation of graphene growth on ni(111), *Surf Sci* 605 (11) (2011) 1095–1098, doi:[10.1016/j.susc.2011.03.011](https://doi.org/10.1016/j.susc.2011.03.011). <http://www.sciencedirect.com/science/article/pii/S0039602811000987>
- [28] K. Takahashi, K. Yamada, H. Kato, H. Hibino, Y. Homma, In situ scanning electron microscopy of graphene growth on polycrystalline ni substrate, *Surf Sci* 606 (7) (2012) 728–732, doi:[10.1016/j.susc.2011.12.009](https://doi.org/10.1016/j.susc.2011.12.009). <http://www.sciencedirect.com/science/article/pii/S003960281100478X>.
- [29] G. Dong, J.W.M. Frenken, Kinetics of graphene formation on rh(111) investigated by in situ scanning tunneling microscopy, *ACS Nano* 7 (8) (2013) 7028–7033, doi:[10.1021/nm402229](https://doi.org/10.1021/nm402229). PMID: 23829447
- [30] Z.-J. Wang, J. Dong, L. Li, G. Dong, Y. Cui, Y. Yang, W. Wei, R. Blume, Q. Li, L. Wang, X. Xu, K. Liu, C. Barroo, J.W.M. Frenken, Q. Fu, X. Bao, R. Schlg, F. Ding, M.-G. Willinger, The coalescence behavior of two-dimensional materials revealed by multiscale in situ imaging during chemical vapor deposition growth, *ACS Nano* 14 (2) (2020) 1902–1918, doi:[10.1021/acsnano.9b08221](https://doi.org/10.1021/acsnano.9b08221). PMID: 32031780
- [31] M. Huang, R.S. Ruoff, Growth of single-layer and multilayer graphene on cu/mi alloy substrates, *Acc. Chem. Res.* 53 (4) (2020) 800–811, doi:[10.1021/acs.accounts.9b00643](https://doi.org/10.1021/acs.accounts.9b00643).
- [32] Y. Hou, B. Wang, L. Zhan, F. Qing, X. Wang, X. Niu, X. Li, Surface crystallographic structure insensitive growth of oriented graphene domains on cu substrates, *Mater. Today* 36 (2020) 10–17, doi:[10.1016/j.mattod.2019.12.001](https://doi.org/10.1016/j.mattod.2019.12.001).
- [33] S. Plimpton, Fast parallel algorithms for short-range molecular dynamics, *J Comput Phys* 117 (1) (1995) 1–19, doi:[10.1006/jcph.1995.1039](https://doi.org/10.1006/jcph.1995.1039). <http://www.sciencedirect.com/science/article/pii/S002199918571039X>
- [34] K. Chenoweth, A.C.T. van Duin, W.A. Goddard, ReaxFF reactive force field for molecular dynamics simulations of hydrocarbon oxidation, *The Journal of Physical Chemistry A* 112 (5) (2008) 1040–1053, doi:[10.1021/jp079896w](https://doi.org/10.1021/jp079896w). PMID: 18197648
- [35] H. Hattab, A.T. N'Diaye, D. Wall, G. Jnawali, J. Coraux, C. Busse, R. van Gastel, B. Poelsema, T. Michely, F.-J. Meyer zu Heringdorf, M. Horn-von Hoegen, Growth temperature dependent graphene alignment on ir(111), *Appl Phys Lett* 98 (14) (2011) 141903, doi:[10.1063/1.3548546](https://doi.org/10.1063/1.3548546).
- [36] A.T. N'Diaye, M. Engler, C. Busse, D. Wall, N. Buckarie, F.-J.M.Z. Heringdorf, R. van Gastel, B. Poelsema, T. Michely, Growth of graphene on ir(111), *New J Phys* 11 (2) (2009) 023006, doi:[10.1088/1367-2630/11/2/023006](https://doi.org/10.1088/1367-2630/11/2/023006).

- [37] S. Zhu, P. Pochet, H.T. Johnson, Controlling rotation of two-dimensional material flakes, *ACS Nano* 13 (6) (2019) 6925–6931, doi:[10.1021/acsnano.9b01794](https://doi.org/10.1021/acsnano.9b01794).
- [38] H. Tetlow, J. Posthuma de Boer, I.J. Ford, D.D. Vvedensky, D. Curcio, L. Omini-cuolo, S. Lizzit, A. Baraldi, L. Kantorovich, Ethylene decomposition on ir(111): initial path to graphene formation, *Phys. Chem. Chem. Phys.* 18 (2016) 27897–27909, doi:[10.1039/C6CP03638D](https://doi.org/10.1039/C6CP03638D).
- [39] Z. Zhang, Y. Yang, F. Xu, L. Wang, B.I. Yakobson, Unraveling the sinuous grain boundaries in graphene, *Adv Funct Mater* 25 (3) (2015) 367–373, doi:[10.1002/adfm.201403024](https://doi.org/10.1002/adfm.201403024).
- [40] J. Li, B. Ni, T. Zhang, H. Gao, Phase field crystal modeling of grain boundary structures and growth in polycrystalline graphene, *J Mech Phys Solids* 120 (2018) 36–48, doi:[10.1016/j.jmps.2017.12.013](https://doi.org/10.1016/j.jmps.2017.12.013). Special issue in honor of Ares J. Rosakis on the occasion of his 60th birthday
- [41] E. Annevelink, E. Ertekin, H.T. Johnson, Grain boundary structure and migration in graphene via the displacement shift complete lattice, *Acta Mater* 166 (2019) 67–74, doi:[10.1016/j.actamat.2018.12.030](https://doi.org/10.1016/j.actamat.2018.12.030).
- [42] H.A. Khater, A. Serra, R.C. Pond, J.P. Hirth, The disconnection mechanism of coupled migration and shear at grain boundaries, *Acta Mater* 60 (5) (2012) 2007–2020, doi:[10.1016/j.actamat.2012.01.001](https://doi.org/10.1016/j.actamat.2012.01.001).
- [43] S. Kurasch, J. Kotakoski, O. Lehtinen, V. Skkalov, J. Smet, C.E. Krill, A.V. Krasheninnikov, U. Kaiser, Atom-by-atom observation of grain bound-ary migration in graphene, *Nano Lett.* 12 (6) (2012) 3168–3173, doi:[10.1021/nl301141g](https://doi.org/10.1021/nl301141g), PMID: 22554303
- [44] A.W. Robertson, G.-D. Lee, K. He, Y. Fan, C.S. Allen, S. Lee, H. Kim, E. Yoon, H. Zheng, A.I. Kirkland, J.H. Warner, Partial dislocations in graphene and their atomic level migration dynamics, *Nano Lett.* 15 (9) (2015) 5950–5955, doi:[10.1021/acsnanolett.5b02080](https://doi.org/10.1021/acsnanolett.5b02080), PMID: 26313338
- [45] J. Kotakoski, J.C. Meyer, Mechanical properties of polycrystalline graphene based on a realistic atomistic model, *Phys. Rev. B* 85 (2012) 195447, doi:[10.1103/PhysRevB.85.195447](https://doi.org/10.1103/PhysRevB.85.195447).
- [46] D. Neas, P. Klapetek, Gwyddion: an open-source software for SPM data analysis, *Open Physics* 10 (1) (2012) 181–188, doi:[10.2478/s11534-011-0096-2](https://doi.org/10.2478/s11534-011-0096-2).
- [47] A.C.T. van Duin, S. Dasgupta, F. Lorant, W.A. Goddard, ReaxFF: a reactive force field for hydrocarbons, *The Journal of Physical Chemistry A* 105 (41) (2001) 9396–9409, doi:[10.1021/jp004368u](https://doi.org/10.1021/jp004368u).
- [48] T.P. Senftle, S. Hong, M.M. Islam, S.B. Kylasa, Y. Zheng, Y.K. Shin, C. Junkermeier, R. Engel-Herbert, M.J. Janik, H.M. Aktulga, T. Verstraelen, A. Grama, A.C.T. van Duin, The reaxFF reactive force-field: development, applications and future directions, *npj Comput. Mater.* 2 (1) (2016) 15011, doi:[10.1038/npjcompumats.2015.11](https://doi.org/10.1038/npjcompumats.2015.11).